Supporting Information

Charge Selective Surface-Enhanced Raman Scattering Using Silver and Gold Nanoparticles Deposited on Silicon-Carbon Core-Shell Nanowires

Sun Young Baik, Yong Jae Cho, Young Rok Lim, Hyung Soon Im, Dong Myung Jang, Yoon Myung, Jeunghee Park,* and Hong Seok Kang*

Table S1. SERS detection limits of dyes for Ag NP and Au NP deposited NW substrates. The log value of the intensity as a function of concentration (in log value) is linearly fitted. We assume that the detection limit (M) is reached when the signal to noise (S/N) ratio is 5. The value of selectivity is estimated from the ratio of the detection limit of the paired substrates.

	R6G		**AO**		**FL**		**MO**	
	Detection limit	Selectivity	Detection limit	Selectivity	Detection limit	Selectivity	Detection limit	Selectivity
Ag-C	3.2×10^{-13}	1	2.3×10^{-11}	1	7.6×10^{-11}	2200	3.6×10^{-11}	6700
Ag-CN	1.9×10^{-15}	170	8.6×10^{-14}	270	1.7×10^{-7}	1	2.4×10^{-7}	1
Au-C	2.4×10^{-11}	1	3.4×10^{-11}	1	9.9×10^{-11}	44	1.4×10^{-9}	1.3
Au-CN	1.2×10^{-11}	2	2.6×10^{-13}	130	4.4×10^{-9}	1	1.8×10^{-9}	1
Ag-pSi	9.7×10^{-14}	1	2.1×10^{-10}	1	5.1×10^{-18}	6.7×10^{8}	4.8×10^{-14}	2.5×10^{5}
Ag-nSi	7.8×10^{-16}	120	1.2×10^{-19}	1.8×10^{9}	3.4×10^{-9}	1	1.2×10^{-8}	1
Au-pSi	3.9×10^{-12}	1	1.3×10^{-8}	1	1.3×10^{-11}	40	2.0×10^{-11}	1
Au-nSi	6.1×10^{-14}	64	2.1×10^{-12}	6200	5.2×10^{-10}	1	2.5×10^{-11}	1.2

Figure S1: SEM and TEM images and EDX data; (a)~(c) Au-CN and (d)~(f) Au-Si.

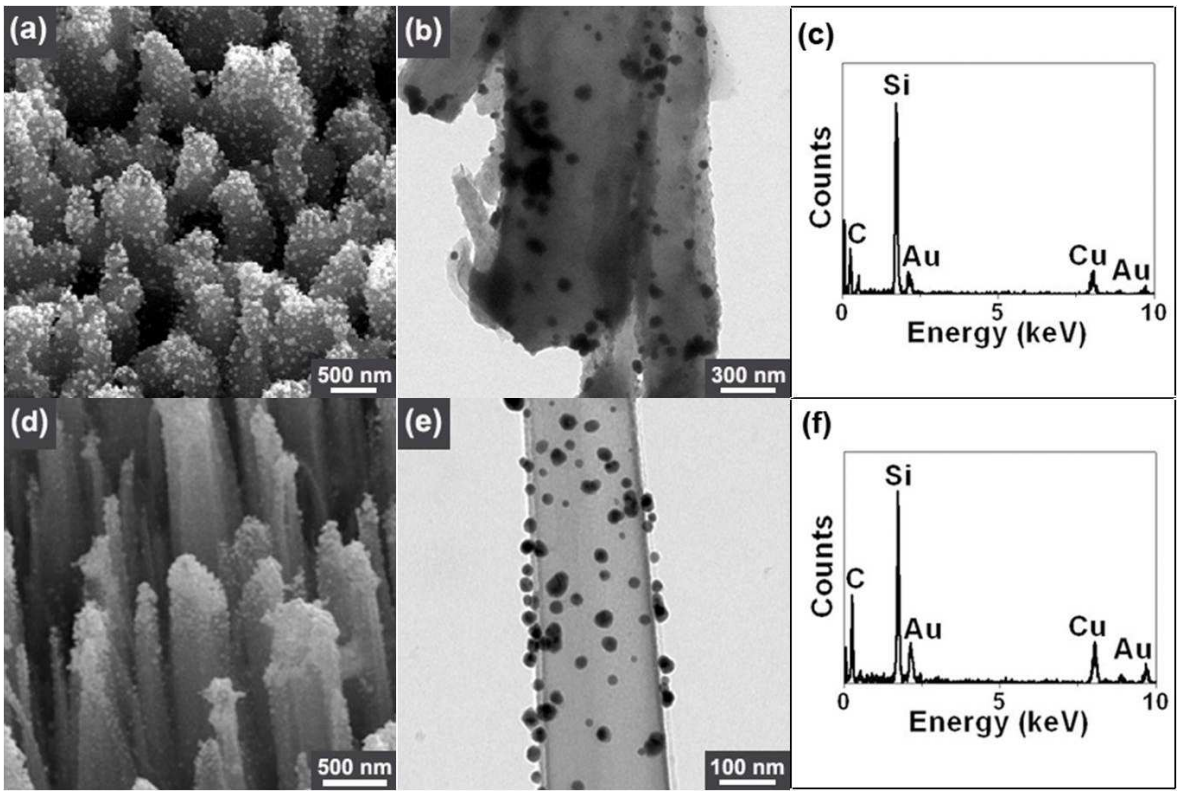

Figure S2: SERS as a function of concentration of R6G for Ag-C.

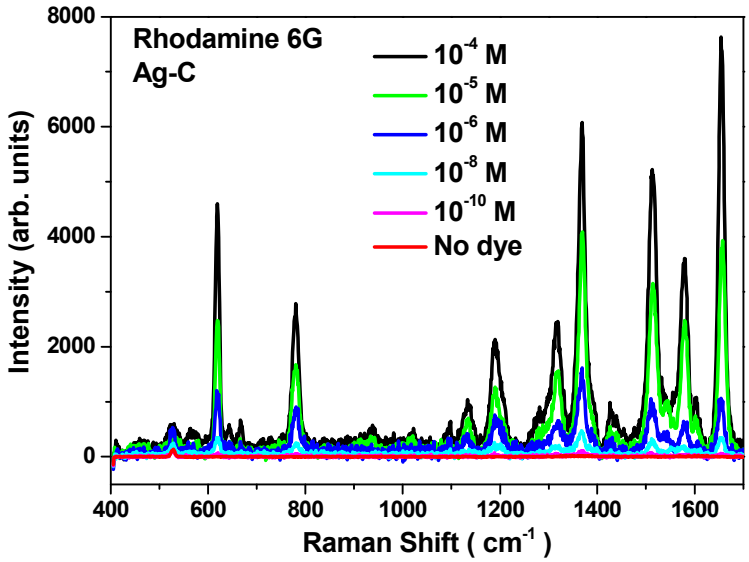

Figure S3: SERS intensity as a function of concentration, (a) R6G, (b) AO, (c) FL, and (d) MO, for Ag-C and Ag-CN.

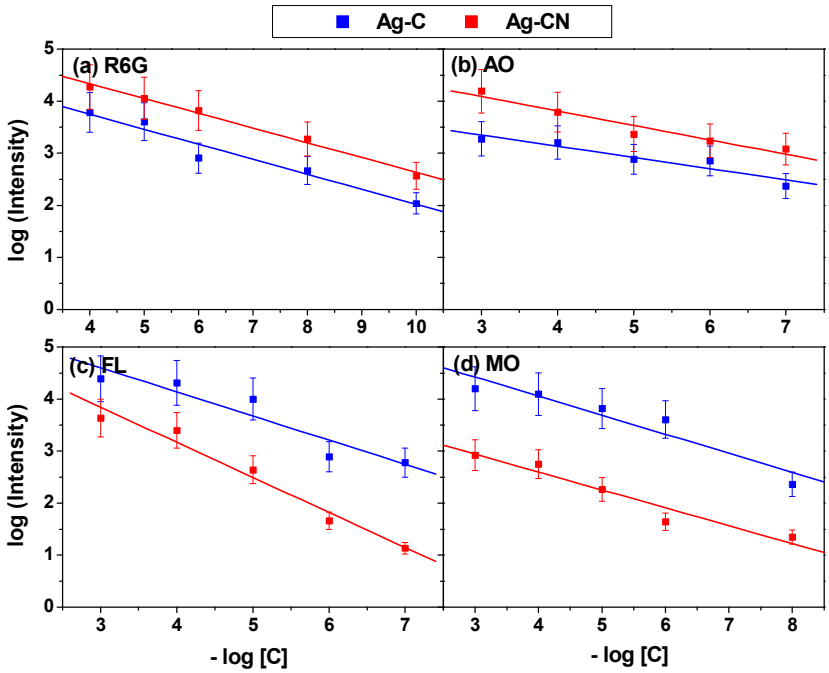

Figure S4: SERS intensity as a function of concentration, (a) R6G, (b) AO, (c) FL, and (d) MO, for the Au-C and Au-CN.

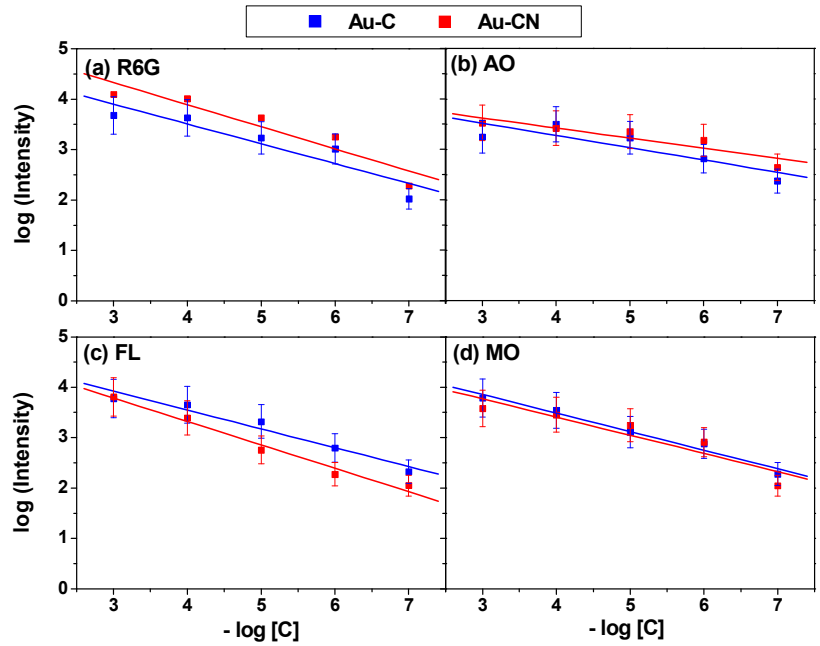

Figure S5: SERS intensity as a function of concentration, (a) R6G, (b) AO, (c) FL, and (d) MO, for the Ag-pSi and Ag-nSi.

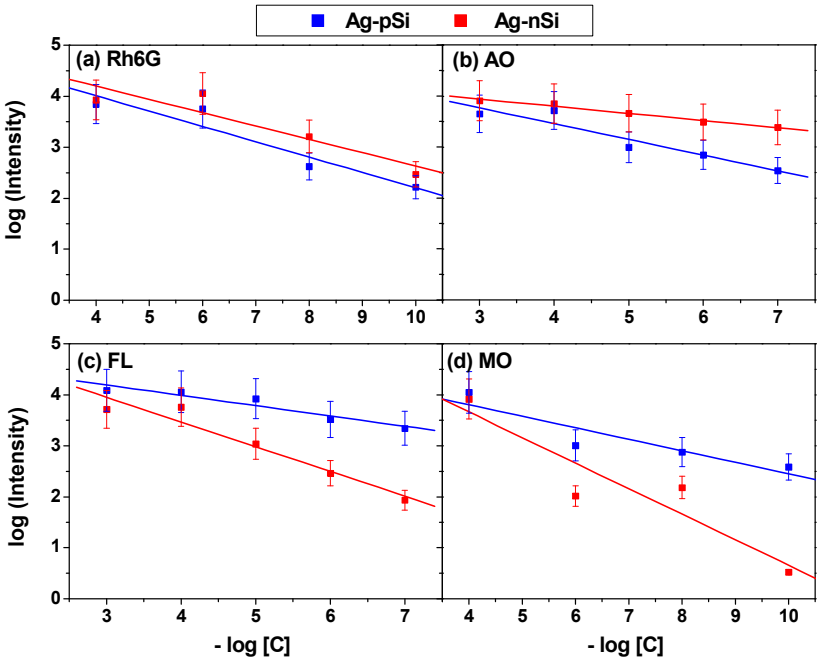

Figure S6: SERS of (a) R6G, (b) AO, (c) FL, and (d) MO dyes for the Au-pSi and Au-nSi, recorded under the same conditions where the concentration is 10^{-6} M. The excitation wavelength is 514.5 nm from an Ar ion laser.

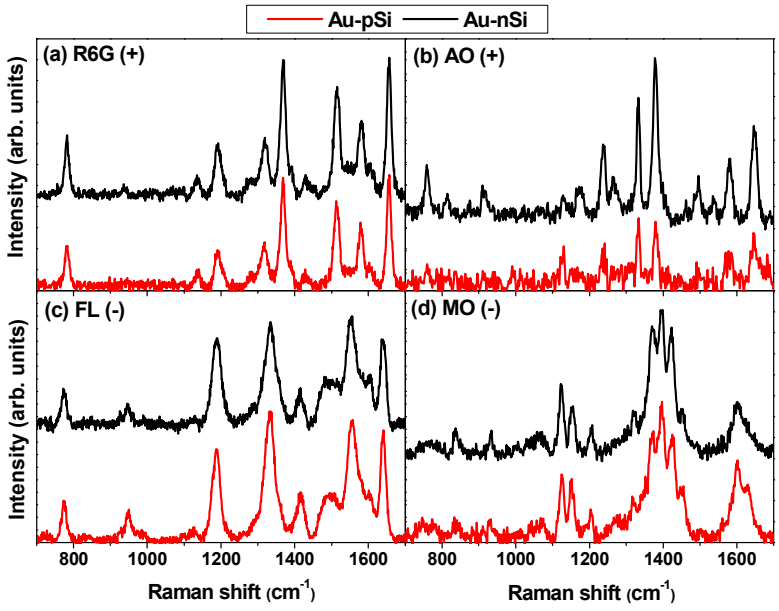

Figure S7: SERS intensity as a function of concentration, (a) R6G, (b) AO, (c) FL, and (d) MO, for the Au-pSi and Ag-nSi.

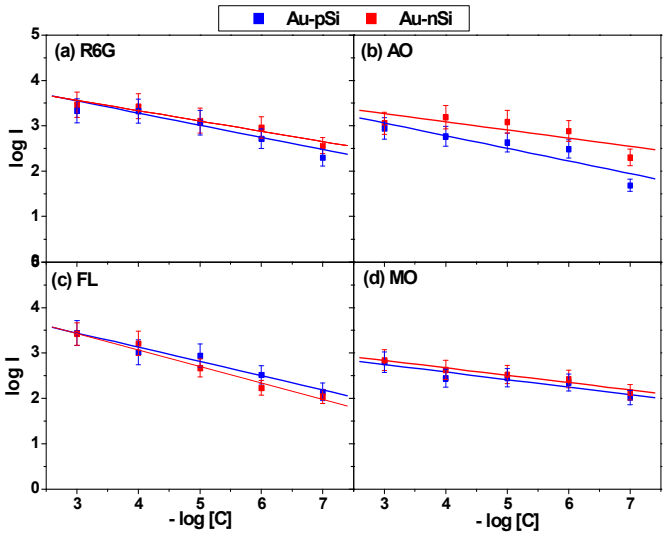

Figure S8: SERS of MO on (b) Ag-nSi and (b) Ag-pSi as a function of the NW length; (c) plot of SERS intensity (at 1397 cm^{-1}) versus the length.

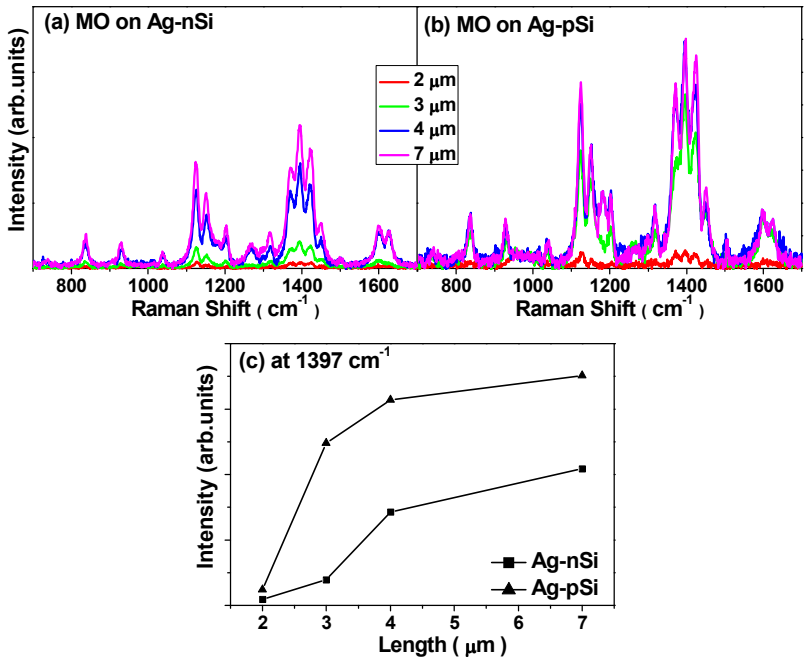

Figure S9: XPS data of Ag and Au NP-deposited Si NWs; (a) Ag $3d_{5/2}$ and (b) Au $4f_{7/2}$. The binding energy of Ag-pSi and Ag-nSi shifts to a lower energy compared to that of the metal by 0.3 eV. The binding energy of Au-pSi and Au-nSi shifts to a lower energy from that of the metal by 0.9 eV. There is a negligible difference in the peak shift for the *n*- and *p*-type Si NWs. The FWHMs are 0.9 and 1.1 eV for the Ag-pSi and Ag-nSi and 0.8 and 1.1 eV for the Au-pSi and Au-nSi, respectively. The broader energy distribution of the *n*-type Si may be correlated with the larger interaction with the NPs, following the more efficient electron transfer. The binding energy of the Si peak exhibits a negligible change in the shift and broadening upon the deposition of the NPs (not shown here).

Previous works on Ag-ZnO nanostructures consistently showed a significant XPS peak shift to the lower binding energy region (0.8 eV) for Ag NPs deposited on *n*-type ZnO NPs.[1] The lower energy binding energy shift of the Au NPs was also observed for *n*-type SnO_2 (1.3 eV), *n*-type CdS (0.5 eV), and *p*-type Cu_2S (0.15 eV).[2-4] The peak shift could be understood by the electron transfer based on the Fermi energy level alignment of the semiconductor and metal. However, other factors such as surface oxide layers and electronegativity are involved in the peak shift, which makes it complicated to predict.

1 Zheng, Y.; Zheng, L.; Zhan, Y.; Lin, X.; Zheng, Q.; Wei, K. Ag/ZnO Heteronanostructure Nanocrystals: Synthesis, Characterization, and Photocatalyst. *Inorg. Chem.* **2007**, *46*, 6980-6986.

2 Yu, K.; Wu, Z.; Zhao, Q.; Li, B. Xie, Y. High-Temperature-Stable Au@SnO_2 Core/Shell Supported Catalyst for CO Oxidation. *J. Phys. Chem. C* **2008**, *112*, 2244-2247.

3 Yang, T.-T.; Chen, W.-T.; Hsu, Y.-J.; Wei, K.-H.; Lin, T.-Y.; Lin, T.-W. Interfacial Charge Carrier Dynamics in Core-Shell Au-CdS Nanocrystals. *J. Phys. Chem. C* **2010**, *114*, 11414-11420.

4 Kim, Y.; Park, K. Y.; Jang, D. M.; Song, Y. M.; Kim, H. S.; Cho, Y. J.; Myung, Y.; Park, J. Synthesis of Au-Cu_2S Core-Shell Nanocrystals and Their Photocatalytic and Electrocatalytic Activity. *J. Phys. Chem. C* **2010**, *114*, 22141-22146.

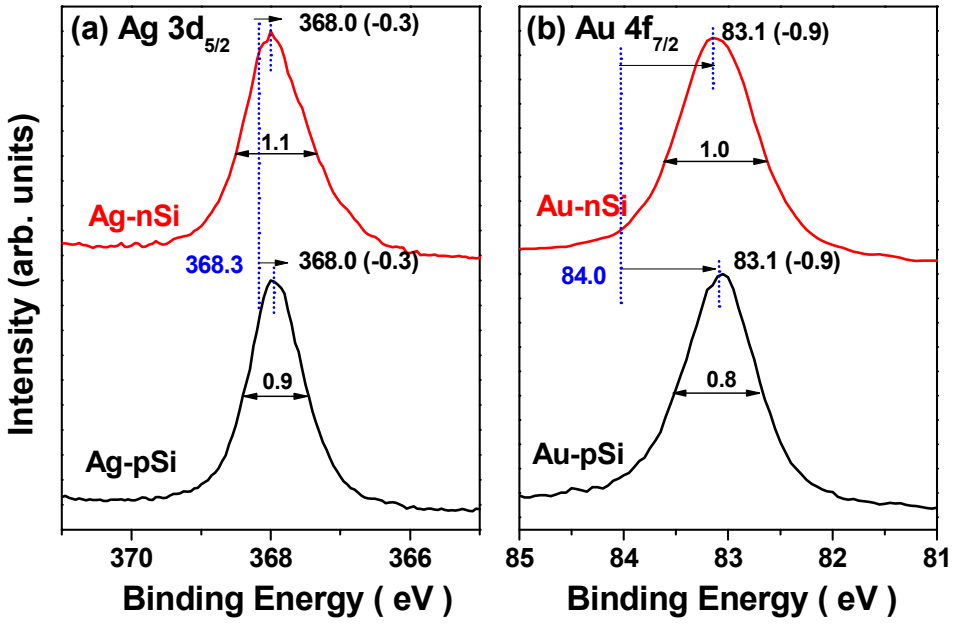

Figure S10: SERS of (a) R6G, (b) AO, (c) FL, and (d) MO dyes for the Si-C and Si-CN core-shell NW (no NP deposition), recorded under the same conditions where the concentration is 10^{-4} M. The excitation wavelength is 514.5 nm from an Ar ion laser.

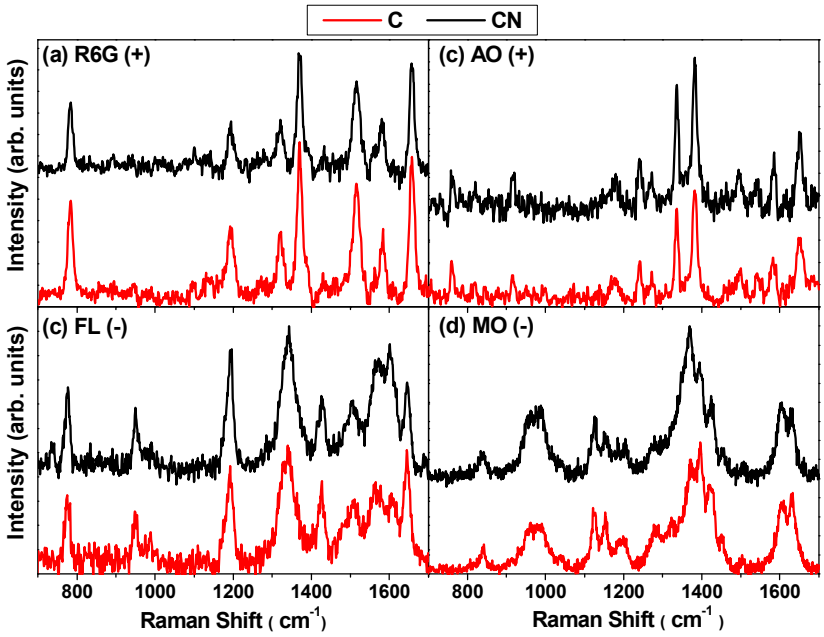

Figure S11. P_z component of the PDOS for all atoms belonging to the N-Gr in the (a) free-standing N-Gr, (b) (N-Gr)-Ag(111) adduct and (c) (N-Gr)-Au(111) adduct. The N doping of the free-standing Gr brings about a large (~ 0.89 eV) upward shift of the Fermi level, with a splitting of the two degenerate bands due to the breaking of the symmetry. Although the PDOS is broadened, the adsorption of Ag on the N-Gr clearly introduces a *p*-type doping effect, which is manifested in the downward shift of the Fermi level by ~0.09 eV. There will be a gradual change from the *n*-type to the *p*-type doping effect as the doping concentration increases from 0 to 3.13 %. On the one hand, the PDOS plot of the (N-Gr)-Au adduct does not clearly show such a Fermi level shift. This is because the bond of the N-Gr admix strongly interacts with the Au orbital, which is correlated with the large binding energy of N-Gr and Au (-1.42 eV). The peak of the free-standing N-Gr at -1.17 eV splits into two peaks at -0.93 and -0.84 eV. Two other peaks of the free-standing N-Gr at -0.71 and -0.53 eV shift downward by ~ 0.20 eV. In short, the *p*-type doping effect appears in the (N-Gr)-Ag adduct at a doping concentration of 3.13%.

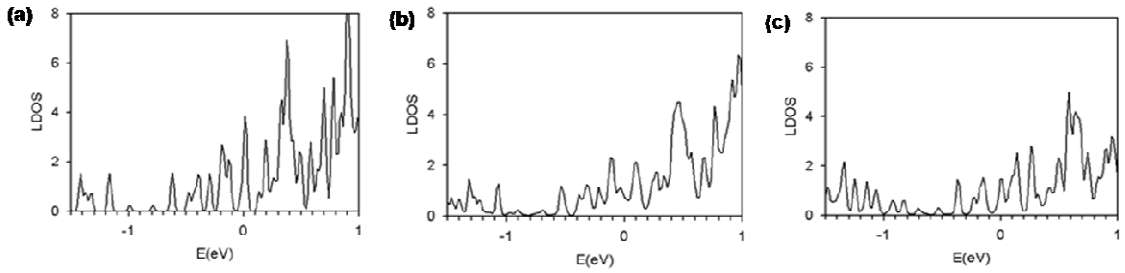

Figure S12. P_z component of the PDOS for all atoms belonging to the P-Gr in the (P-Gr)-Ag(111) adduct: (a) R-R_e=∞, (b) 0.40 Å, and (c) 0.00 Å; and in the (P-Gr)-Au(111) adduct: (e) R-R_e = 0.34 Å and (f) 0.00 Å. The PDOS of the (P-Gr)-Ag adduct at various inter-planar separations (R) shows a large upward shift of the Fermi level as the P-Gr approaches the Ag (111) surface along a vertical direction. The strong peak of the free-standing P-Gr at 0.94 eV splits into two peaks in the (P-Gr)-Ag. Therefore, we estimated the Fermi level shift based on the energy position of the middle of these two peaks. The shifts are 0.47 and 0.77 eV at R-R_{eq}=0.40 and 0.00 Å, respectively, where R_{eq} is the equilibrium separation of the minimized energy adduct. For the (P-Gr)-Au adduct, there is also an upward shift of the Fermi level as the separation becomes shorter. The level shifts upward by 0.16 and 0.39 eV at R-Re = 0.34 and 0.00 Å, respectively. Therefore, the P-Gr will apparently experience an *n*-type doping effect upon the adsorption of Ag or Au, irrespective of the N atom concentration, if we assume that the rigid charge transfer model applies.